

Numerical simulation of electron energy loss near inhomogeneous dielectrics

F. J. García de Abajo

Departamento de CCIA, Facultad de Informática, UPV/EHU, Apartado 649, 20080 San Sebastián, Spain

J. Aizpurua

Departamento de Física de Materiales, Facultad de Química, UPV/EHU, Apartado 1072, 20080 San Sebastián, Spain

(Received 7 July 1997; revised manuscript received 22 August 1997)

The nonrelativistic energy loss suffered by fast electrons passing near dielectric interfaces of arbitrary shape is calculated by solving Poisson's equation using the boundary-charge method. The potential induced by a moving electron is expressed in terms of surface-charge distributions placed at the interfaces. These surface charges, obtained by self-consistently solving the resulting integral equation, act back on the electron producing a retarding force and hence energy loss. The dielectrics are described by frequency-dependent dielectric functions. Two particular cases are discussed in further detail: interfaces invariant under translation along one particular direction and axially symmetric interfaces. Previous results for simple geometries, such as planes, spheres, and cylinders, based upon analytical solutions, are fully reproduced within this approach. Calculations are presented for electrons moving near wedges, coupled parallel cylinders, coupled spheres, and toroidal surfaces. [S0163-1829(97)00848-5]

I. INTRODUCTION

Sophisticated numerical simulation of the elastic scattering contribution to image contrast is routinely employed in conventional high-resolution electron microscopy of inhomogeneous materials. Inelastic scattering effects are usually included only via a complex optical potential.^{1,2} Now that increasing numbers of high-resolution microscopes are fitted with energy-loss imaging facilities, a much wider interest in inelastic scattering processes, hitherto mainly the preserve of scientists equipped with scanning transmission electron microscopes, can be anticipated with a consequent requirement to be able to interpret loss intensities in terms of local chemical and electronic structure. For energy-loss events above about 50 eV, involving the excitation of characteristic atomic levels, existing theory can broadly satisfy these requirements even if the computation of the details of edge shapes in inhomogeneous regions may still present challenging problems. For the relatively more intense, valence loss region the situation is so far much less satisfactory because the theory has to deal with collective excitations as well as with the delocalization arising from the larger impact parameters permissible in low-energy transfers. Fermi's nonrelativistic theory³ of dielectric excitation by a moving classical electron has been successfully extended to deal with inhomogeneous situations in simple geometries such as planes,⁴⁻⁶ cylinders,⁷⁻⁹ parabolic wedges,¹⁰ and spheres,^{11,12} where the solutions (essentially of Laplace's equation) can be calculated analytically. Approximate solutions that have been obtained for more complex geometries such as hemispheres,¹³ coupled sphere and plane,^{14,15} coupled spheres,^{16,17} or coupled cylinders¹⁸ are still based on increasingly elaborate analytical analysis. There is an obvious need for direct numerical simulation methods enabling valence losses to be computed in arbitrary geometries using standard packages.

A promising basis for such a numerical approach is the boundary-charge method, also known as the boundary-

element method,¹⁹ whereby a distribution of surface or interface charges is generated, interacting self-consistently with itself as well as with any external field, such as that due to a passing electron. This approach can be traced back to Maxwell,²⁰ who used it to compute capacitances, but it has been employed much more recently to determine normal mode frequencies of dielectric excitations by Fuchs^{21,22} for a cube and by Ouyang and Isaacson²³ for bodies of arbitrary shape. Ouyang and Isaacson²⁴ have gone on to apply the boundary method to investigate the effect of the support on fast electron energy losses near small particles, but do not provide many details of their procedures. Other recent applications of this approach include the surface modes of channels cut on planar surfaces²⁶ and those of coupled parallel wires.²⁷

Frequency-dependent dielectric functions will be used to describe the responses of different media in what follows. Atomic units (a.u., $e = m = \hbar = 1$) will be used from now on, unless otherwise specified.

Section II will be devoted to the description of the method. The particular case of cylindrical interfaces (i.e., those that are translationally invariant along one particular direction but otherwise arbitrarily shaped) will be considered in Sec. III, where calculations of the loss probability of electrons passing near wedges and coupled parallel cylinders is offered. Axially symmetric interfaces will be analyzed in Sec. IV, with numerical application to the cases of several coupled spheres and toroidal surfaces. Finally, the conclusions will be summarized in Sec. V.

II. BASIC THEORY

A. Boundary-charge method

Within the local response approximation, the Poisson equation that relates the scalar potential $\phi(\mathbf{r}, \omega)$ to the external charge density distribution $\rho^{\text{ext}}(\mathbf{r}, \omega)$ in the presence of inhomogeneous dielectrics can be written

$$\nabla[\epsilon(\mathbf{r}, \omega) \nabla \phi(\mathbf{r}, \omega)] = -4\pi \rho^{\text{ext}}(\mathbf{r}, \omega), \quad (1)$$

where the dielectric response is described in terms of an arbitrary function of space \mathbf{r} and frequency ω , $\epsilon(\mathbf{r}, \omega)$. Equation (1) can be recast

$$\phi(\mathbf{r}, \omega) = \phi^\infty(\mathbf{r}, \omega) + \phi^{\text{boundary}}(\mathbf{r}, \omega), \quad (2)$$

where

$$\phi^\infty(\mathbf{r}, \omega) = \int d\mathbf{r}' \frac{\rho^{\text{ext}}(\mathbf{r}', \omega)}{\epsilon(\mathbf{r}', \omega) |\mathbf{r} - \mathbf{r}'|} \quad (3)$$

and

$$\phi^{\text{boundary}}(\mathbf{r}, \omega) = \frac{1}{4\pi} \int d\mathbf{r}' \frac{\nabla \phi(\mathbf{r}', \omega) \cdot \nabla \epsilon(\mathbf{r}', \omega)}{\epsilon(\mathbf{r}', \omega) |\mathbf{r} - \mathbf{r}'|}. \quad (4)$$

The first term in Eq. (2) reduces to the bulk screened potential in infinitely extended homogeneous materials. The second term originates in the inhomogeneity of the response function; it will reduce to surface integrals in the case of homogeneous dielectrics separated by abrupt interfaces. We shall focus on this kind of systems from now on.

The different homogeneous dielectrics will be labeled by an index μ . Denoting $\epsilon_\mu(\omega)$ the dielectric function characterizing medium μ , the full space- and frequency-dependent dielectric function reads

$$\epsilon(\mathbf{r}, \omega) = \sum_\mu \epsilon_\mu(\omega) \theta_\mu(\mathbf{r}),$$

where $\theta_\mu(\mathbf{r})$ is 1 when \mathbf{r} lies in medium μ , 1/2 on its boundary, and 0 otherwise.

The integrand in Eq. (4) is nonzero only at the interfaces, where the dielectric function suffers a sudden variation, conveniently described in terms of surface δ functions. One can write

$$\frac{1}{4\pi} \frac{\nabla \phi \cdot \nabla \epsilon}{\epsilon} = \frac{1}{4\pi} \mathbf{D} \cdot \nabla \frac{1}{\epsilon} = \sigma \delta_S, \quad (5)$$

where δ_S is the surface delta function that defines the interfaces,

$$\sigma(\mathbf{s}, \omega) = \frac{1}{4\pi} \frac{\epsilon_{\mu_1}(\omega) - \epsilon_{\mu_2}(\omega)}{\epsilon_{\mu_1}(\omega) \epsilon_{\mu_2}(\omega)} \mathbf{n}_s \cdot \mathbf{D}(\mathbf{s}, \omega) \quad (6)$$

is the induced boundary charge, \mathbf{s} is the coordinate vector running over the interfaces, \mathbf{n}_s is the interface normal at \mathbf{s} , and the indices μ_1 and μ_2 refer to the media lying opposite the interface normal and in the direction of the interface normal, respectively (see Fig. 1). Obviously, those indices may depend on \mathbf{s} . Notice that in deriving Eq. (6) from Eq. (5), the δ function in the latter is unambiguously defined thanks to the continuity of the component of the electric displacement normal to the interface $\mathbf{n}_s \cdot \mathbf{D}$.

Using Eq. (6), Eq. (4) reduces to

$$\phi^{\text{boundary}}(\mathbf{r}, \omega) = \int d\mathbf{s} \frac{\sigma(\mathbf{s}, \omega)}{|\mathbf{r} - \mathbf{s}|}. \quad (7)$$

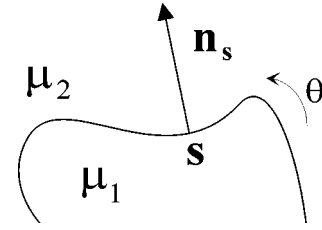


FIG. 1. Schematic representation of an interface separating media μ_1 and μ_2 . The normal \mathbf{n}_s at the interface position \mathbf{s} has been chosen to point towards medium μ_2 [see Eq. (6)]. The small curved arrow indicates the sense of increasing parameter θ .

If the external charge ρ^{ext} does not present singularities at the interface, the electric field produced by ϕ^∞ is continuous. However, this is not the case of the electric field derived from ϕ^{boundary} . The analysis of this contribution is more subtle. According to the Gauss theorem, for \mathbf{s} and \mathbf{s}' lying on the interface one has

$$\lim_{t \rightarrow 0^+} \mathbf{n}_s \cdot \nabla (1/|\mathbf{s} \pm t \mathbf{n}_s - \mathbf{s}'|) = F(\mathbf{s}, \mathbf{s}') \mp 2\pi \delta(\mathbf{s} - \mathbf{s}'),$$

where

$$F(\mathbf{s}, \mathbf{s}') = - \frac{\mathbf{n}_s \cdot (\mathbf{s} - \mathbf{s}')}{|\mathbf{s} - \mathbf{s}'|^3}$$

and the limit corresponds to approaching the interface from medium μ_2 and μ_1 for upper and lower signs, respectively. F gives rise to a continuous contribution to the electric field. The normal electric field at a point of medium μ_2 infinitesimally close to the interface can then be written $-\mathbf{n}_s \cdot \nabla \phi(\mathbf{s}, \omega) + 2\pi \sigma(\mathbf{s}, \omega)$ and hence the normal displacement reads

$$\mathbf{n}_s \cdot \mathbf{D}(\mathbf{s}, \omega) = \epsilon_{\mu_2}(\omega) [-\mathbf{n}_s \cdot \nabla \phi(\mathbf{s}, \omega) + 2\pi \sigma(\mathbf{s}, \omega)],$$

where $-\nabla \phi(\mathbf{s}, \omega)$ refers to the continuous part of the electric field noted above. Combining this expression with Eq. (6) and using Eqs. (3) and (7), one finds

$$\Lambda(\omega) \sigma(\mathbf{s}, \omega) = \mathbf{n}_s \cdot \nabla \phi^\infty(\mathbf{s}, \omega) + \int d\mathbf{s}' F(\mathbf{s}, \mathbf{s}') \sigma(\mathbf{s}', \omega), \quad (8)$$

where

$$\Lambda(\omega) = 2\pi \frac{\epsilon_{\mu_2}(\omega) + \epsilon_{\mu_1}(\omega)}{\epsilon_{\mu_2}(\omega) - \epsilon_{\mu_1}(\omega)}. \quad (9)$$

Equation (8) constitutes a self-consistent relation for σ . The dimension of the problem is reduced from 3 in Eq. (1) to 2 in Eq. (8), with the consequent reduction in the number of points employed to numerically solve it.²⁷ It is the aim of this work to provide expressions suitable for the numerical evaluation of integral equation (8).

B. Solution in terms of interface modes

The self-sustained oscillations of the system are described by

$$2\pi\lambda_i\sigma^i(\mathbf{s}) = \int d\mathbf{s}' F(\mathbf{s}, \mathbf{s}')\sigma^i(\mathbf{s}'), \quad (10)$$

where i labels the different modes. The operator F is not symmetric in general. Nevertheless, Ouyang and Isaacson have shown that its eigenvalues λ_i are real.²⁵ Moreover, the eigenfunctions σ^i form a complete basis set that satisfies the orthogonality property

$$\int d\mathbf{s} \int d\mathbf{s}' \frac{\sigma^i(\mathbf{s}) \sigma^j(\mathbf{s}')^*}{|\mathbf{s} - \mathbf{s}'|} = \delta_{ij}, \quad (11)$$

where the normalization has been conveniently chosen.

Now the inhomogeneous term of Eq. (8) can be expanded in this basis set as

$$\mathbf{n}_s \cdot \nabla \phi^\infty(\mathbf{s}, \omega) = \sum_{i,\mu} \frac{1}{\epsilon_\mu(\omega)} f_{i\mu}(\omega) \sigma^i(\mathbf{s}),$$

where

$$f_{i\mu}(\omega) = \int d\mathbf{s} \int d\mathbf{s}' \mathbf{n}_s \cdot \nabla \phi_\mu^{\text{ext}}(\mathbf{s}, \omega) \frac{\sigma^i(\mathbf{s}')^*}{|\mathbf{s} - \mathbf{s}'|}$$

and

$$\phi_\mu^{\text{ext}}(\mathbf{s}, \omega) = \int_{V_\mu} d\mathbf{r} \frac{\rho^{\text{ext}}(\mathbf{r}, \omega)}{|\mathbf{s} - \mathbf{r}|}$$

is the direct potential created by the external charge contained in medium μ .

Finally, the solution of Eq. (8) can be written

$$\sigma(\mathbf{s}, \omega) = \sum_{i,\mu} \frac{C_{i\mu}}{\epsilon_\mu(\omega)} \sigma^i(\mathbf{s}) \quad (12)$$

and the coefficients $C_{i\mu}$ are determined by solving

$$\sum_{j,l} \Lambda_l \sigma_l^{ij} C_{j\mu} = f_{i\mu} + 2\pi\lambda_i C_{i\mu}, \quad (13)$$

where l labels different interfaces, so that Λ_l depends on the two media that interface l actually separates [see Eq. (9)] and

$$\sigma_l^{ij} = \int d\mathbf{s} \int_{S_l} d\mathbf{s}' \frac{\sigma^i(\mathbf{s})^* \sigma^j(\mathbf{s}')}{|\mathbf{s} - \mathbf{s}'|},$$

where the integral in \mathbf{s}' is restricted to interface l . Notice that $\sum_l \sigma_l^{ij} = \delta_{ij}$, according to Eq. (11).

In the particular case where only two different media are considered, $\mu=1,2$, the index l can be disregarded in the equations written above. Then Eqs. (12) and (13) are readily solved and the surface charge reduces to

$$\sigma(\mathbf{s}, \omega) = \sum_{i,\mu} \frac{f_{i\mu}}{\epsilon_\mu(\omega)[\Lambda(\omega) - 2\pi\lambda_i]} \sigma^i(\mathbf{s}). \quad (14)$$

Notice that the frequency of the self-sustained modes are related to the eigenvalues λ_i via the dielectric functions of the two media according to $\Lambda(\omega) = 2\pi\lambda_i$. Apell and co-workers²⁸ have exploited this relationship to derive sum rules connecting the modes of a system to that obtained by interchanging the dielectric properties of both media, and the

modes of interacting subsystems to those of the noninteracting subsystems. Notice that for certain geometries (e.g., the dielectric sphere), F is positively or negatively defined (i.e., its eigenvalues are all positive or negative), leading to natural oscillation frequencies always below or above the flat surface mode, respectively.

C. Electron-energy-loss probability

All of the above can be applied to arbitrary external perturbations. Let us now focus on a fast electron moving with constant velocity \mathbf{v} along a straight-line trajectory described by $\mathbf{r} = \mathbf{r}_0 + \mathbf{v}t$, where \mathbf{r}_0 is the particle position at $t=0$. The rate of energy loss suffered by the electron can be expressed in terms of the induced force acting on it according to

$$\begin{aligned} \frac{dE}{dt} &= \mathbf{v} \cdot \nabla \phi^{\text{ind}}(\mathbf{r}, t)|_{\mathbf{r}=\mathbf{r}_0+\mathbf{v}t} \\ &= \frac{d\phi^{\text{ind}}(\mathbf{r}_0 + \mathbf{v}t, t)}{dt} - \frac{\partial}{\partial t} \phi^{\text{ind}}(\mathbf{r}, t)|_{\mathbf{r}=\mathbf{r}_0+\mathbf{v}t}. \end{aligned} \quad (15)$$

The first term on the right-hand side of this equation represents a conservative work, which need not be considered here; it vanishes when integrated over an infinite trajectory passing near a finite target and also for an electron beam directed parallel to a cylindrical surface of the sort discussed below. The second term accounts for production of real excitations in the target, that is, the dissipative part of the work, and thus it will be denoted dE^{diss}/dt . It can be decomposed into the contribution of different energy losses ω in the following way:

$$\Delta E^{\text{diss}} = \int dt \left(\frac{dE^{\text{diss}}}{dt} \right) = \int_0^\infty \omega d\omega \Gamma(\omega),$$

where

$$\Gamma(\omega) = \frac{1}{\pi} \int dt \text{Im} \{ -\phi^{\text{ind}}(\mathbf{r}_0 + \mathbf{v}t, \omega) e^{-i\omega t} \} \quad (16)$$

is the loss probability per unit energy ω . This can in turn be conveniently separated as

$$\Gamma = \Gamma^\infty + \Gamma^{\text{boundary}},$$

where Γ^∞ corresponds to bulk losses [coming from the induced part of Eq. (3)] and Γ^{boundary} is related to losses originating in the interface modes [obtained by substituting Eq. (7)] for ϕ^{ind} in Eq. (16).

For the fast electron considered above, the external charge density reads

$$\rho^{\text{ext}}(\mathbf{r}, \omega) = \delta(\mathbf{r}^\perp - \mathbf{r}_0^\perp) \frac{e^{i(r^\parallel - r_0^\parallel)\omega/v}}{v},$$

where \mathbf{r}^\perp and r^\parallel represent the components of \mathbf{r} perpendicular and parallel to \mathbf{v} , respectively. The bulk losses are readily found to be

$$\Gamma^\infty(\omega) = \frac{2}{\pi v} \sum_\mu T_\mu \int_{\omega/v}^{2v} \frac{dq}{q} \text{Im} \left\{ \frac{-1}{\epsilon_\mu}(\omega) \right\}, \quad (17)$$

where T_μ represents the time spent by the electron inside medium μ and the upper limit of integration is provided by the cutoff $2v$, which accounts for the maximum momentum that the electron is able to transfer to the target. A more realistic way of calculating bulk losses consists in introducing a dependence of the dielectric function on momentum q .

The bulk losses offer little information on the geometry of the system. The rich structure of coupled modes with frequencies well separated from the bulk plasmon frequencies of the different media that form the target is contained in the surface loss term, on which we are going to focus in what follows. Inserting Eq. (7) into Eq. (16), one finds

$$\Gamma^{\text{boundary}}(\omega) = \frac{-2}{\pi v} \int ds K_0 \left(\frac{\omega |\mathbf{r}_0^\perp - \mathbf{s}^\perp|}{v} \right) \text{Im} \{ \sigma(\mathbf{s}, \omega) e^{i(r_0^\parallel - s^\parallel)\omega/v} \}. \quad (18)$$

The expression for the loss probability is further simplified when only two different materials are considered. Inserting Eq. (14) into Eq. (18), one finds

$$\Gamma^{\text{boundary}}(\omega) = \frac{1}{v^2} \sum_i \sum_{\mu=1}^2 \text{Im} \left\{ - \left[g_i(\omega) - \frac{1}{\epsilon_\mu(\omega)} \right] \Gamma_{i\mu} \right\}, \quad (19)$$

where

$$\Gamma_{i\mu} = \frac{pvf_{i\mu}(\omega)}{2\pi^3(1+p\lambda_i)} \int ds \sigma^i(\mathbf{s}) e^{i(r_0^\parallel - s^\parallel)\omega/v} K_0 \left(\frac{\omega |\mathbf{r}_0^\perp - \mathbf{s}^\perp|}{v} \right), \quad (20)$$

$$g_i(\omega) = \frac{2}{\epsilon_1(\omega)(1+\lambda_i) + \epsilon_2(\omega)(1-\lambda_i)},$$

$p = -1$ ($p = 1$) for $\mu = 1$ ($\mu = 2$), and i labels the different oscillation modes derived from Eq. (10).

An interesting property of Eq. (19) is that it separates the dependence on the dielectric functions from that on the geometry of the system. Actually, the coefficients $\Gamma_{i\mu}$ are independent of the dielectric functions. So, provided one knows these coefficients, it is easy to obtain the loss probability for an arbitrary choice of the response functions. Moreover, $(\omega/v)\Gamma_{i\mu}$ depends on the distances d that characterize the geometry of the trajectory and the geometry of the target only via $\omega d/v$. This scaling property permits one to apply the results of a single calculation to various geometries that differ just in a scaling of distances by a constant factor.

Equation (19) takes a particularly simple form when the electron trajectory is fully contained in one of the media μ_0 , in which case the coefficients $\Gamma_{i\mu_0} \equiv \Gamma_i$ are real and the rest of the coefficients $\Gamma_{i\mu}$ are zero.²³ One obtains

$$\Gamma^{\text{boundary}}(\omega) = \frac{1}{v^2} \sum_i \Gamma_i \text{Im} \left\{ - \left[g_i(\omega) - \frac{1}{\epsilon_{\mu_0}(\omega)} \right] \right\}, \quad (21)$$

where Γ_i is independent of the choice of dielectric functions but depends on the position of the electron beam \mathbf{r}_0^\perp via $\omega \mathbf{r}_0^\perp/v$ and also on the geometry of the interface. The term $-1/\epsilon_{\mu_0}(\omega)$ inside the square brackets of Eq. (21) lowers the loss probability; it represents the begrenzung effect, that is, the fact that the strength of the bulk modes given by Eq. (17) is reduced as some interface mode i is activated. Rather than using Eq. (20) to calculate Γ_i , we will obtain it directly from Eqs. (8) and (18) by using a Drude dielectric function with a damping sufficiently small to ensure that the loss probability at the energy of resonance ω_i comes almost exclusively from mode i . Then, dividing by $g_i(\omega)$ one readily obtains Γ_i .

The following sections will be devoted to showing the range of applicability of the present formalism to actual geometries. Different selected cases will be studied.

III. TRANSLATIONALLY INVARIANT INTERFACES

Let us consider an arbitrarily shaped cylindrical interface parallel to the z direction, described in terms of the parametric curve $\mathbf{R}_s(\theta) = (x_s(\theta), y_s(\theta))$ [i.e., $\mathbf{s}(\theta, z) = (x_s, y_s, z)$ and $d\mathbf{s} = dz d\theta \sqrt{x_s'^2 + y_s'^2}$, where the prime denotes differentiation with respect to the parameter θ]. The interface normal $\mathbf{n}_s = (y_s', -x_s', 0)/\sqrt{x_s'^2 + y_s'^2}$ points towards the medium on the right-hand side when one runs along the interface in the sense of increasing θ , as shown in Fig. 1.

The translational invariance along the z direction makes it natural to work in Fourier space with respect to that direction,

$$\sigma(\theta, z, \omega) = \int \frac{dq}{2\pi} \sigma_q(\theta, \omega) e^{iqz}.$$

This permits one to solve Eq. (8) separately for each q component. In particular, Eq. (3) becomes

$$\phi_q^\infty(\mathbf{R}, \omega) = 2 \int d\mathbf{R}' K_0(|q||\mathbf{R} - \mathbf{R}'|) \frac{\rho_q^{\text{ext}}(\mathbf{R}', \omega)}{\epsilon(\mathbf{R}', \omega)}, \quad (22)$$

where the spatial dependence of the dielectric function $\epsilon(\mathbf{R}, \omega)$ is now limited to the directions perpendicular to the z axis, $\mathbf{R} = (x, y)$. Large- q components are associated with rapidly oscillating eigenfunctions $\sigma_q e^{iqz}$, which cannot “feel” the curvature of the surface and hence their eigenfrequencies pile up near the flat surface frequency ($\lambda_i = 0$).²⁹

Using Eq. (22), the inhomogeneous term of Eq. (8) becomes

$$f_q(\theta, \omega) = \mathbf{n}_s(\theta) \cdot \nabla \phi_q^\infty(\mathbf{R}_s(\theta), \omega) = \int \frac{d\mathbf{R}}{\epsilon(\mathbf{R}, \omega)} H_q(\mathbf{R}, \theta) \rho_q^{\text{ext}}(\mathbf{R}, \omega), \quad (23)$$

where

$$H_q(\mathbf{R}, \theta) = 2|q|K_1[|q||\mathbf{R} - \mathbf{R}_s(\theta)|] \mathbf{n}_s(\theta) \cdot \frac{\mathbf{R} - \mathbf{R}_s(\theta)}{|\mathbf{R} - \mathbf{R}_s(\theta)|}.$$

Finally, Eq. (8) reduces to

$$\Lambda(\omega) \sigma_q(\theta, \omega) = f_q(\theta, \omega) + \int d\theta' F_q(\theta, \theta') \sigma_q(\theta', \omega), \quad (24)$$

where

$$F_q(\theta, \theta') = \sqrt{x'_s(\theta')^2 + y'_s(\theta')^2} H_q(\mathbf{R}_s(\theta'), \theta).$$

Now $\sigma(\theta, \omega)$ can be obtained numerically from Eq. (24). One possibility consists in projecting it onto a suitable orthogonal basis set (e.g., spherical harmonics for spheres), keeping enough terms to reach the required accuracy.^{25,24} We will work rather in real space. Following Lu and Maradudin,²⁶ this integral equation will be solved by discretizing the parameter θ . Rather than a continuous variable, we will consider a convenient partition of the range of θ , that is, a finite set of N intervals, labeled $i = 1 - N$. The length of interval i will be denoted $\Delta\theta_i$ and θ_i will be a representative value of θ inside it. Now the integral in Eq. (24) can be approximated by a sum; one comes to

$$\Lambda(\omega)[\sigma_q]_i = [f_q]_i + \sum_j [F_q]_{i,j}[\sigma_q]_j,$$

where $[\sigma_q]_i = \sigma_q(\theta_i, \omega)$, $[F_q]_{i,j} = F_q(\theta_i, \theta_j)\Delta\theta_j$, and the dependence of σ and f on frequency ω is understood.

Using matrix notation, the solution of Eq. (24) reads

$$\sigma(\theta_i, z, \omega) = \int \frac{dq}{2\pi} e^{iqz} \sum_j \left[\frac{1}{\Lambda(\omega) - F_q} \right]_{i,j} [f_q]_j, \quad (25)$$

where $[1/(\Lambda - F_q)]_{i,j}$ is the (i, j) element of the inverse of matrix $\Lambda - F_q$. Notice that $\Lambda(\omega)$ is a diagonal matrix that may depend on \mathbf{s} via the different kind of media that the interface separates at each particular point, according to Eq. (9).

The discretization procedure relies on the assumption that the quantities σ_q , f_g , and F_q vary very little inside each interval. The dominant contribution to the loss probability of fast electrons comes from the lowest-order modes derived from Eq. (10), modes that do not display rapid oscillations along the interface; hence one expects that σ_q be a smooth function of θ . In addition, f_q can show strong variations near the electron beam when this passes very close to some interface, so that the size of the intervals has to be small in that region. Finally, $F_q(\theta, \theta')$ is finite when $\theta' \rightarrow \theta$ and more precisely

$$\lim_{\theta' \rightarrow \theta} F_q(\theta, \theta') = \frac{y'_s x''_s - x'_s y''_s}{x_s'^2 + y_s'^2}, \quad (26)$$

provided the interface does not have sharp edges; otherwise, F_q presents integrable divergences, which can be handled with using an open formula for the numerical integration³⁰ in the discretization of Eq. (24).

An adaptative choice of $\Delta\theta_i$ is crucial in limiting the total number of intervals N to a minimum. Indeed, more points θ_i are necessary near regions where two interfaces are close together or where their curvature radius is small. For instance, in a wedge, it is essential to accumulate many little intervals near its corner and not so critical to cover the sides in detail. We have quantified this effect with good convergent results by making the length of each interval inversely proportional to the normal component of the electric field that the whole set of interfaces would create on the interval under consideration if they were uniformly charged [i.e., $\Delta\theta_i$

is chosen to be inversely proportional to the average of $F_q(\theta_i, \theta')$ over θ']. In the particular cases considered below convergence has been achieved using $N = 100 - 200$.

The second term on the right-hand side of Eq. (8) vanishes for an isolated flat surface [see Eq. (26)] and the boundary charge method trivially produces the well-known results for this case.⁵ In thin films, where the two surfaces are coupled, full numerical agreement has been found with previous results.³¹ Let us now discuss other more complicated geometries.

A. Energy loss for electrons traveling parallel to the interface

For a unit charge moving along the direction of translational invariance of the cylindrical interface with velocity v and two-dimensional impact parameter $\mathbf{R}_0 = (x_0, y_0)$, one has

$$\rho_q^{\text{ext}}(\mathbf{R}, \omega) = 2\pi \delta(\mathbf{R} - \mathbf{R}_0) \delta(\omega - qv) e^{-i\omega z_0/v},$$

and hence there is only one momentum component contributing to the energy loss, namely $q = \omega/v$. Moreover, the total loss probability Γ is infinite and it only makes sense to talk about loss probability per unit time (i.e., loss rate P). Inserting $\rho_q^{\text{ext}}(\mathbf{R}, \omega)$ into Eq. (23), using Eqs. (18) and (25), and dividing by the interaction time, one finds

$$P^{\text{boundary}}(\omega) = \frac{2}{\pi v} \sum_{i,j} \Delta\theta_i \sqrt{x'_s(\theta_i)^2 + y'_s(\theta_i)^2} \times K_0 \left(\frac{\omega |\mathbf{R}_0 - \mathbf{R}_s(\theta_i)|}{v} \right) \text{Im} \left\{ \frac{-1}{\epsilon_{\mu_0}(\omega)} \times \left[\frac{1}{\Lambda(\omega) - F_{\omega/v}} \right]_{i,j} H_{\omega/v}(\mathbf{R}_0, \theta_j) \right\}, \quad (27)$$

where μ_0 refers to the medium inside of which the charge is moving.

As a first example of application, let us consider a hyperbolic wedge surface described by $x_s y_s = b^2/2$ with $x_s, y_s < 0$, so that b is the distance from its corner to the origin and its asymptotes coincide with the x and y axes. The wedge will be assumed to be surrounded by vacuum and made of a metal of plasma frequency ω_p , characterized by the frequency-dependent Drude dielectric function

$$\epsilon(\omega) = 1 - \frac{\omega_p^2}{\omega(\omega + i\gamma)}.$$

For an electron beam directed parallel to the wedge, Eq. (27) provides the loss rate due to the creation of surface excitations. Some particular spectra have been represented in Figs. 2 and 3 for 100-keV electrons. The plasma frequency has been taken to be $\omega_p = 15.8$ eV and the damping $\gamma = 0.5$ eV, values appropriate for Al.

The dependence on b is illustrated in Fig. 2 when the electron beam moves in the vacuum side and passes at a distance of 30 a.u. from the origin (i.e., $x_0 = y_0 = 21.2$ a.u.). Dobrzynski and Maradudin³² pointed out that the spectrum of a sharp wedge ($b=0$) must be a continuum. Later, Davis²⁹ showed that hyperbolic wedges are characterized by a discrete spectrum formed by even and odd modes, which are symmetric and antisymmetric with respect to the bisector

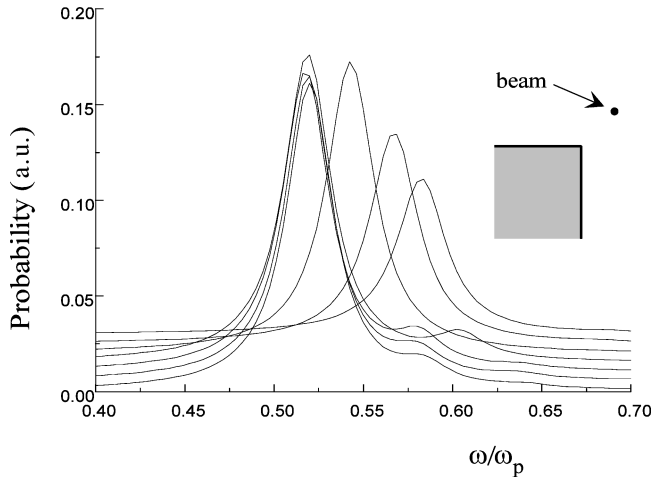


FIG. 2. Loss rate spectra for a 100-keV electron moving parallel to a hyperbolic wedge as a function of b , the distance from its corner to the origin. The asymptotes of the wedge are taken to form an angle of 90° . The electron beam is located on the bisector of the wedge and in the vacuum side at a distance of 30 a.u. from the origin in all cases, as shown in the inset. The values of b are 0.001, 0.01, 0.1, 1, 10, 30, and 50 a.u. (every curve has been shifted upward 0.005 a.u. with respect to the previous one for clarity). The wedge is described by the Drude dielectric function with $\omega_p = 15.8$ eV and damping $\gamma = 0.5$ eV.

of the wedge, respectively. The dominant feature observed in Fig. 2, hereafter denoted corner peak, corresponds to an energy loss of $\approx \omega_p/2$ for small values of b and shifts towards higher energies for increasing b , in agreement with the first of the even modes obtained by Davis.²⁹ When $b \rightarrow 0$, the lowest-order even modes pile up near $\omega_p/2$ and the odd modes near $0.85\omega_p$; higher-order modes of frequencies very

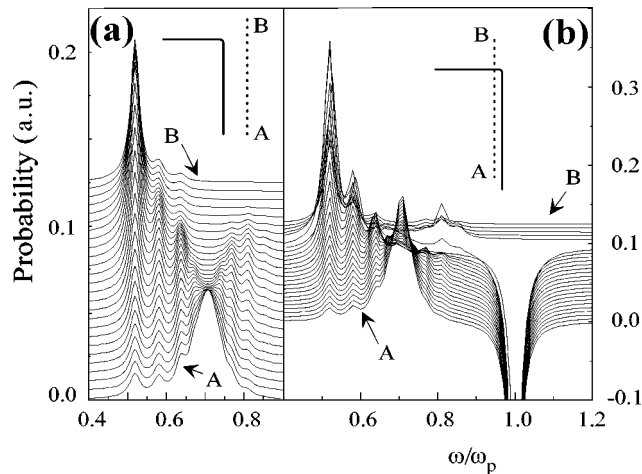


FIG. 3. Dependence of the loss rate $P(\omega)$ on the position of the electron beam under the same conditions as in Fig. 2 for $b = 0.01$ a.u. Different spectra correspond to equally separated positions of the beam along lines parallel to one of the wedge asymptotes, as shown in the insets. The spectra evolve smoothly between both ends of those lines, designated A and B, respectively, and whose coordinates are (in a.u.) (a) (50, -200) and (50, 50) and (b) (-20, -200) and (-20, 50) respectively. The electron travels in the vacuum side for all cases in (a) and inside the wedge for some trajectories in (b).

different from these values cannot be efficiently excited by the electron beam since they correspond to very rapidly oscillating σ_q eigenfunctions.

Figures 3(a) and 3(b) represent the evolution of the loss spectra as the ion beam sweeps a line parallel to the x axis (see the insets). We have taken $\omega b/v = 0.01$. The intensity of the corner peak, relevant near the corner of the wedge, decreases when the beam is near one of the sides, where the classical surface plasmon of a flat surface, $\omega_s = \omega_p/\sqrt{2}$, becomes the dominant frequency. Inside the material [Fig. 3(b)], the surface contribution P^{boundary} has a negative value near ω_p , due to the begrenzung effect. Of course, when the bulk losses are added, the total loss probability is positive. Notice the emergence of a small peak at $\omega \approx 0.83\omega_p$ when the beam is close to the surface; this comes from the excitation of the first odd mode.

The allowed momentum transfer q is fixed in the parallel trajectories: $q = \omega/v$. This permits one to tune modes corresponding to a given choice of q by varying the electron velocity. It is interesting to stress that the above results are the same for other combinations of v and b such that $\omega b/v$ remains constant, due to the scaling property discussed in Sec. II C. In addition, the wedge replicates itself under transformation of distance scaling if $b = 0$, and the results obtained for $b < 1$ for the impact parameter under consideration in Fig. 2 can be applied to that case since no variation with b is observed below that value.

The contribution to the total loss probability coming from each surface mode can be used in combination with the scaling property just noted to obtain loss probabilities for arbitrary choices of dielectric functions and absolute scales according to Eq. (21). As discussed above, the total loss probability diverges for the geometries under consideration, so that Eq. (21) has to be replaced by the loss rate

$$P^{\text{boundary}}(\omega) = \frac{1}{v} \sum_i P_i \text{Im} \left\{ - \left[g_i(\omega) - \frac{1}{\epsilon_{\mu_0}(\omega)} \right] \right\}$$

(notice the different scaling with v). Figure 4–6 offer some examples of P_i for different modes of various targets, obtained from Eq. (10). They should be understood as energy filtered images in the case of small damping γ .

The contour plots shown in Figs. 4 and 5 correspond to the same geometry as in Fig. 2 for $\omega b/v = 0.1$ and $\omega b/v = 0.001$, respectively. The weight of different modes in the loss rate P_i is represented for the first two symmetric modes in (a) and (c) ($n = 0$ and 2, respectively) and the first two antisymmetric modes in (b) and (d) ($n = 1$ and 3, respectively). The accompanying plots show the mode eigenfunctions σ_q^i directly over the surface profile. The number of changes of sign of σ_q^i is given by n . Notice that the mode $n = 0$ (corner mode) acts preferentially near the wedge corner, in agreement with the spectra discussed above.

The smooth curvature of the corner in the wedge studied in Fig. 4 is clearly observable both in σ_q^i and in the contour plots. Notice, for instance, how the corner spot in Fig. 4(c) is displaced towards the actual corner from the origin, where the bright regions in Fig. 4(b) point at.

For the small value of b considered in Fig. 5, the surface charge of the first modes accumulates close to the corner

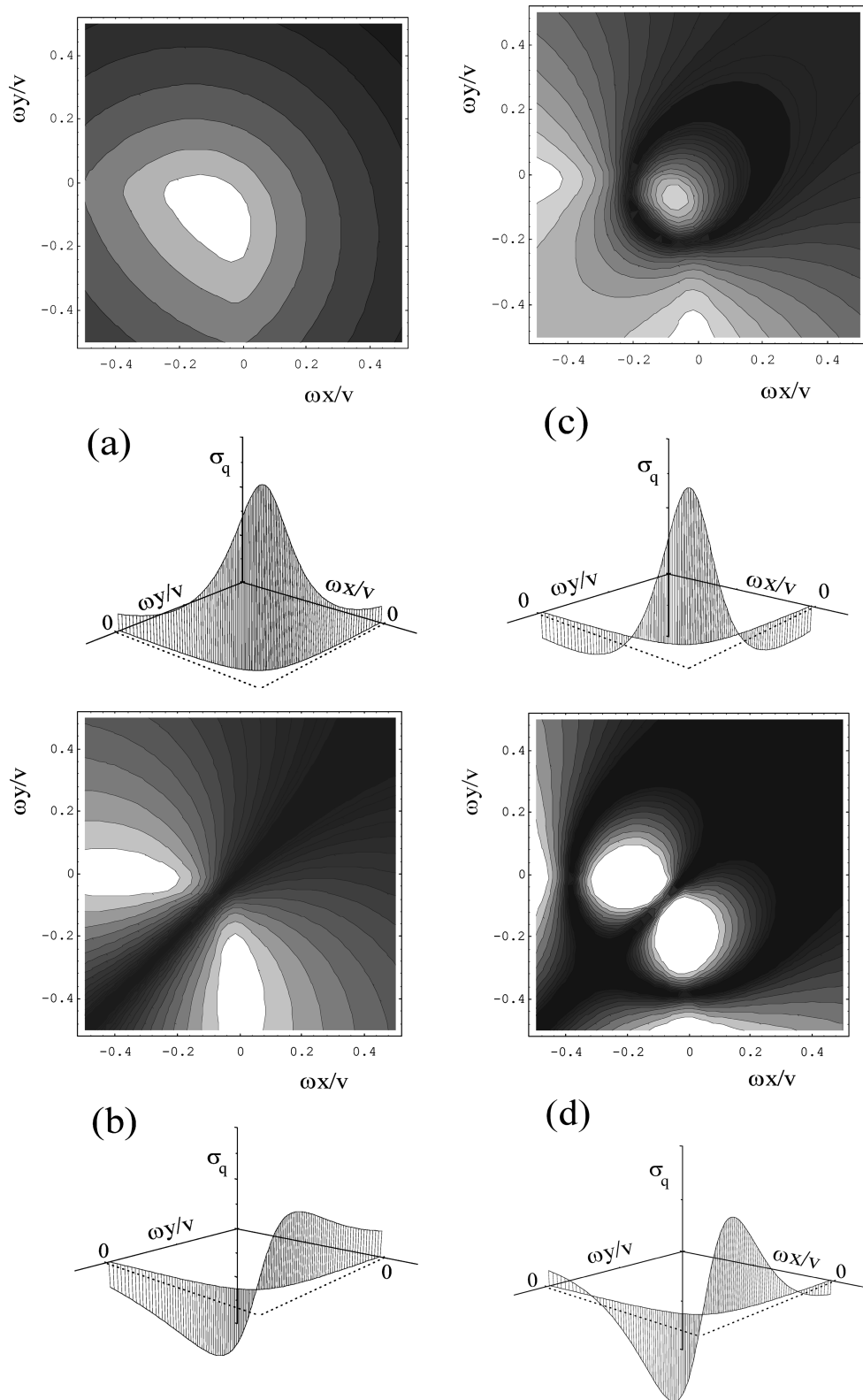


FIG. 4. The weight P_i that multiplies the contribution of the first two symmetric modes [(a) and (c), respectively] and the first two antisymmetric modes [(b) and (d), respectively] to the total loss rate of an electron traveling parallel to a wedge surface is represented here as a function of $x\omega/v$ and $y\omega/v$. They correspond to $\lambda_i = -0.371, 0.190, -0.101,$ and 0.053 for (a)-(d), respectively. The contour lines limiting white areas stand for $P_i = 1.13, 0.27, 0.17,$ and 0.27 , respectively. The darker the region, the smaller the value of P_i . The distance between consecutive contour lines corresponds to a factor of $2/3$. The wedge is contained in the $x, y < 0$ region and its asymptotes are made to coincide with the x and y axes. The distance from the corner to the origin is set equal to $b\omega/v = 0.1$. The inset accompanying each contour plot shows the density associated with the mode under consideration σ_q^i , with $q = \omega/v$, represented directly on the surface profile.

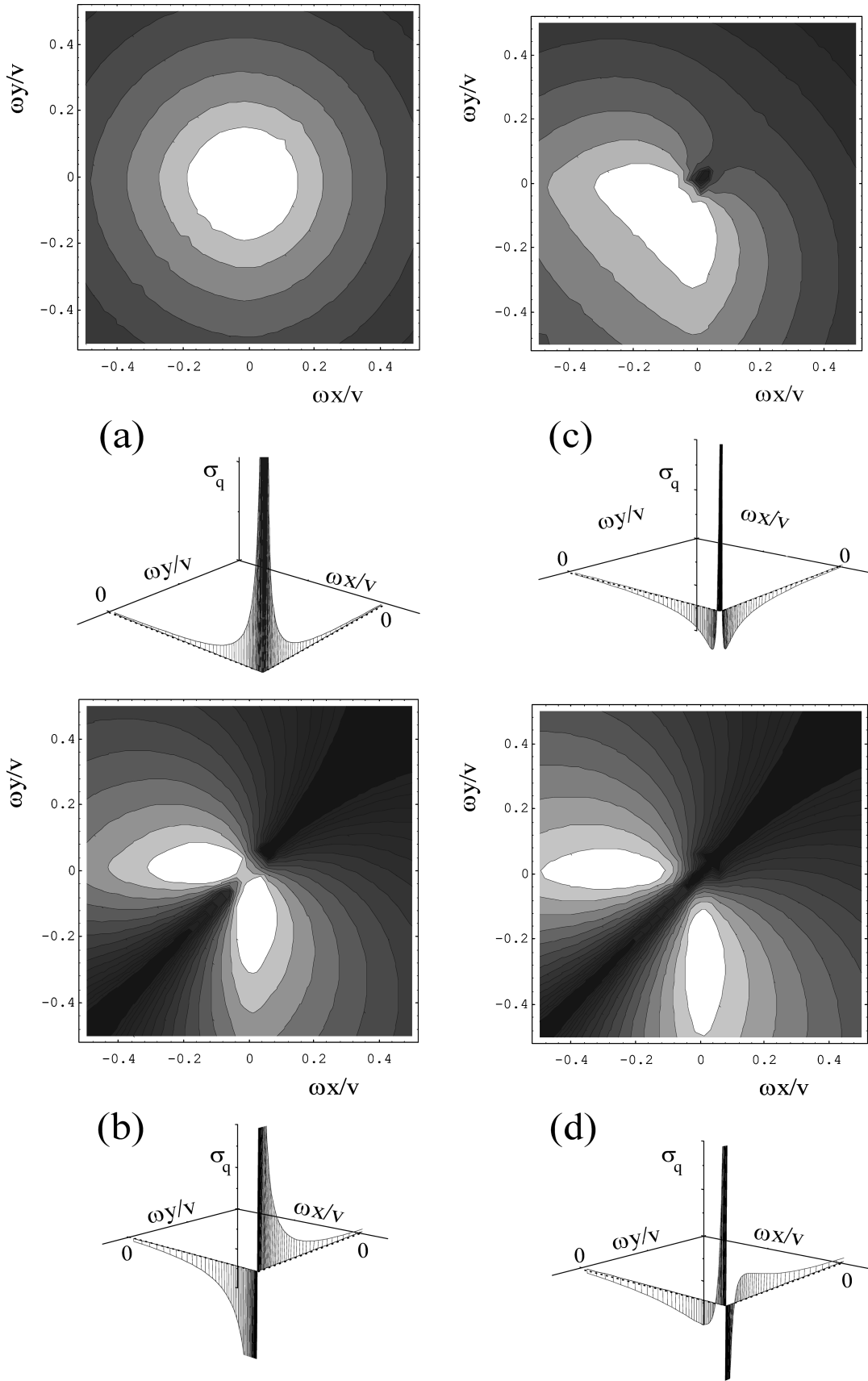


FIG. 5. Same as Fig. 4 for $b\omega/v=0.001$. The values of λ_i are now $-0.451, 0.409, -0.324,$ and $0.257,$ respectively, and those of P_i in the contour lines limiting white regions are $1.33, 0.12, 0.36,$ and $0.12,$ respectively.

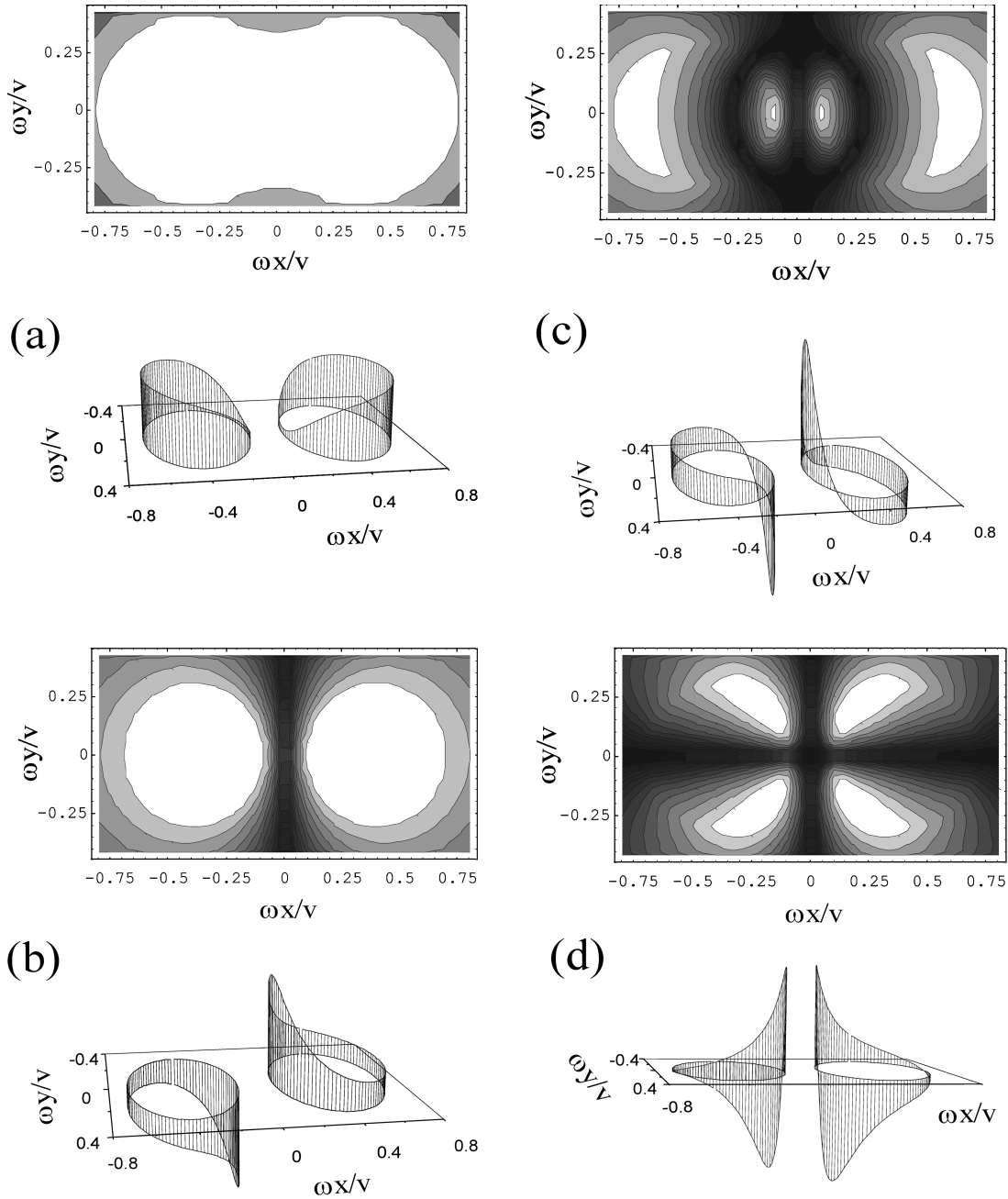


FIG. 6. Same as Fig. 4 for two parallel cylinders of radius $R\omega/v=0.3$ whose centers are separated by a distance $a\omega/v=0.8$. The values of λ_i are (a) -0.830 , (b) -0.938 , (c) -0.242 , and (d) -0.225 . The values of P_i in the contour lines limiting white areas are 0.42 , 0.20 , 0.18 , and 0.15 , respectively. The insets represent σ_q^i directly on the surface profiles for each mode.

(compare the plots of σ_q^i with those of Fig. 4) and the contour plot of the corner peak is nearly circular [Fig. 5(a)]. An obvious spatial correlation between bright regions in the contour plots on the one hand and the peaks of σ_q^i in the accompanying insets on the other can be clearly observed, except in the peaks near the corner of the wedge in Figs. 5(c) and 5(d), too narrow to contribute to efficiently excite their respective modes.

Figure 6 illustrates the case of two neighboring circular cylinders, whose surfaces are described by $(x_s \pm a/2)^2 + y_s^2 = R^2$. The symmetric mode shown in Fig. 6(a) gives the largest contribution to the loss, though the image coming out of it does not permit one to establish the

geometry of the object. The image corresponding to the first antisymmetric mode [Fig. 6(b)] clearly reflects the shape of the two cylinders. Unlike these two modes, higher order modes can only be excited efficiently near the cylinder surfaces, as can be seen in Figs. 6(c) and 6(d).

B. Energy loss for electrons traveling perpendicularly to the interface

Next we shall examine the case of perpendicular motion. Let us consider a fast electron moving with velocity v parallel to the x direction along the straight line defined by $z=0$ and $y=a$. The external charge density that represents this electron is given by

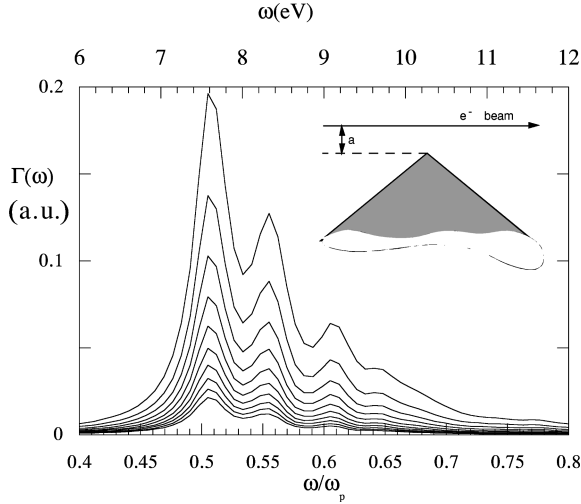


FIG. 7. Loss probability for a 100-keV electron traveling perpendicularly to a hyperbolic wedge as depicted in the inset. Different impact parameters have been considered with respect to the wedge corner, ranging from 10 a.u. to 190 a.u. in steps of 20 a.u. (the larger the distance to the wedge, the lower the probability). The distance from the corner to the origin has been taken to be $a = 0.01$ a.u. The wedge is described by the Drude dielectric function with $\omega_p = 15.8$ eV and damping $\gamma = 0.5$ eV.

$$\rho_q^{\text{ext}}(\mathbf{R}, \omega) = \frac{1}{v} e^{i\omega x/v} \delta(y-a).$$

Assuming for simplicity that the particle moves fully inside medium μ_0 without crossing any interface, Eq. (23) reduces to

$$f_q^\perp(\theta, \omega) = \frac{2\pi}{vQ} \frac{e^{i\omega x_s/v}}{\epsilon_{\mu_0}(\omega)} \frac{e^{-Q|a-y_s|}}{\sqrt{x_s'(\theta)^2 + y_s'(\theta)^2}} \times \left[\frac{i\omega}{v} y_s' - Q x_s' \text{sgn}(a-y_s) \right], \quad (28)$$

where $Q = \sqrt{q^2 + w^2/v^2}$.

The first term on the right-hand side of Eq. (15), which represents a conservative work, vanishes after integration along the whole trajectory. Thus the total loss probability per unit ω is found to be

$$\Gamma(\omega) = \frac{1}{\pi} \int dt \text{Im}\{ -\phi^{\text{ind}}(vt, a, 0, \omega) e^{-i\omega t} \}.$$

Finally, using Eqs. (18), (25), and (28), one obtains

$$\Gamma^{\text{boundary}}(\omega) = \frac{2}{\pi v} \int_0^\infty \frac{dq}{Q} \sum_{i,j} \Delta \theta_i \times \sqrt{x_s'(\theta_i)^2 + y_s'(\theta_i)^2} e^{-Q|a-y_s(\theta_i)|} \times \text{Im} \left\{ e^{-i\omega x_s(\theta_i)/v} \left[\frac{-1}{\Lambda(\omega) - F_q} \right]_{i,j} [f_q^\perp]_j \right\}. \quad (29)$$

Figure 7 shows spectra corresponding to trajectories directed perpendicularly to the wedge, as shown in the inset.

They have been obtained from Eq. (29). The corner peak is again the dominant feature. Smaller peaks can be seen near $\omega \approx 0.56\omega_p$, $0.61\omega_p$, and $0.65\omega_p$. These roughly agree with the position of the modes found for the wedge from Eq. (10), though these results cannot be ascribed to a single value of q , as in the case of parallel trajectories, since the electron does not conserve its momentum along the direction of motion [see the integral over q in Eq. (29)]. However, the dominant value of q is still given by ω/v (compare the position of the corner peak with the case of parallel trajectories in Fig. 2 for $b = 0.01$ a.u.).

IV. AXIALLY SYMMETRIC INTERFACES

Interfaces characterized by axial symmetry are conveniently described in cylindrical coordinates, so that $\mathbf{s}(\theta, \phi) = (\rho_s(\theta)\cos\phi, \rho_s(\theta)\sin\phi, z_s(\theta))$, where ρ_s is the distance to the z axis and θ is a parameter.

Using Fourier series to represent the dependence on the azimuthal angle ϕ , the surface charge can be expressed as

$$\sigma(\mathbf{s}, \omega) = \frac{1}{2\pi} \sum_m \sigma_m(\theta, \omega) e^{im\phi}, \quad (30)$$

where m labels different Fourier components. Moreover, the integral equation (8) becomes totally identical to Eq. (24), except that the momentum q has to be replaced by the integer m . The kernel of the integral is found to be

$$F_m(\theta, \theta') = \rho_s(\theta') \sqrt{x_s'(\theta')^2 + y_s'(\theta')^2} \times \int d\varphi \frac{A - C\cos\varphi}{(B - D\cos\varphi)^{3/2}},$$

where

$$A = n_\rho \rho_s(\theta) - n_z [z_s(\theta) - z_s(\theta')],$$

$$B = \rho_s(\theta)^2 + \rho_s(\theta')^2 + [z_s(\theta) - z_s(\theta')]^2,$$

$$C = n_\rho \rho_s(\theta'), \quad D = 2\rho_s(\theta)\rho_s(\theta'),$$

and $(n_\rho, n_z) = (z_s'(\theta), -\rho_s'(\theta))/\sqrt{\rho_s'(\theta)^2 + z_s'(\theta)^2}$ stands for the radial and z components of the interface normal.

For simplicity, we will consider electron trajectories parallel to the axis of symmetry and fully contained inside one of the dielectrics μ_0 . In that case, the inhomogeneous term of Eq. (24) is found to be

$$f_m(\theta, \omega) = \frac{-4\pi\omega}{v^2 \epsilon_{\mu_0}(\omega)} e^{i\omega z/v} \left(I_m \left\{ \frac{\omega a}{v} \left[n_\rho K_m' \left(\frac{\omega \rho_s(\theta)}{v} \right) \right] \times i n_z K_m \left(\frac{\omega \rho_s(\theta)}{v} \right) \right\} \theta(\rho_s(\theta) - a) \right) + K_m \left\{ \frac{\omega a}{v} \left[n_\rho I_m' \left(\frac{\omega \rho_s(\theta)}{v} \right) \right] i n_z I_m \left(\frac{\omega \rho_s(\theta)}{v} \right) \right\} \times \theta(a - \rho_s(\theta)) \right),$$

where a is the distance from the trajectory to the z axis.

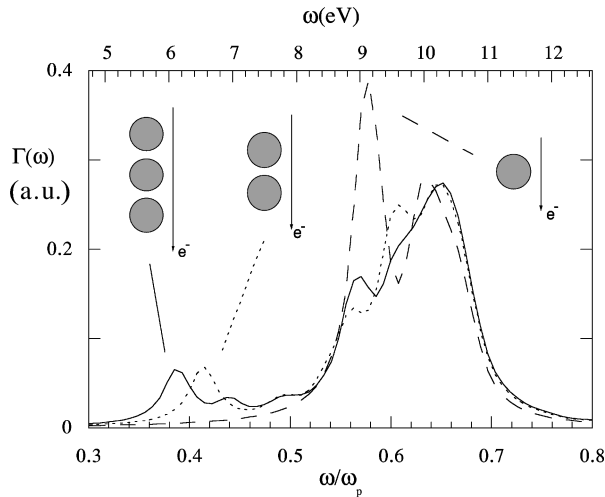


FIG. 8. Loss probability suffered by 100-keV electrons moving parallel to systems of one to three spheres aligned along the direction of motion of the electrons. The spheres are surrounded by vacuum and assumed to be made of Al, described via the Drude dielectric function for $\omega_p = 15.8$ eV and damping $\gamma = 0.5$ eV. The radii of the spheres are all equal to 10 nm. The electron passes at a distance of 1 nm from the sphere surfaces. Neighboring spheres are separated 0.833 nm. The probability has been divided by the number of spheres under consideration. The insets represent the geometry of the target, including arrows that show the electron trajectory.

The different m components of the surface charge (30) are decoupled and their contribution to the loss can be calculated separately. High-order terms decrease rapidly with m and their oscillation frequencies go to ω_s . It has been found that the contribution of $m > 6$ is negligible in the cases considered below.

Figure 8 shows the loss probability experienced by an electron passing close to coupled Al spheres. The loss per sphere has been calculated for systems of spheres aligned along the direction of motion of the electron (see the insets for a schematic description of the geometry). The position of the energy-loss peaks agrees well with previous calculations for the two-sphere system.^{33,16} The results for the loss near isolated spheres¹¹ and recent calculations based on analytical expansion in terms of bispherical coordinates for the two-sphere system^{16,17} are reproduced within the present approach. The low-energy peak at around 6 eV, which emerges in that case, is split into two peaks when one passes to the three-sphere system. The small bump at around 7.5 eV remains the same and the peak near 9 eV is enhanced.

As a final example, motivated by the increasing number of nanostructures that are becoming experimentally available, we have explored the loss near a Al torus. Figure 9(a) shows the results for different impact parameters. When the electron passes near the center of the torus, the main contribution to the energy loss comes from $\omega \approx 0.84\omega_p$, which is related to the excitation of the $m=0$ component in Eq. (30). A richer structure is obtained in external trajectories, for which the loss probability due to different m components has been analyzed in Fig. 9(b). Notice that the contribution of each component cannot be assigned to a single frequency. In particular, the excitation of the $m=0$ component induces losses around $\omega \approx 0.67\omega_p$, in contrast to what happens with trajectories passing near the center. This is similar to the case

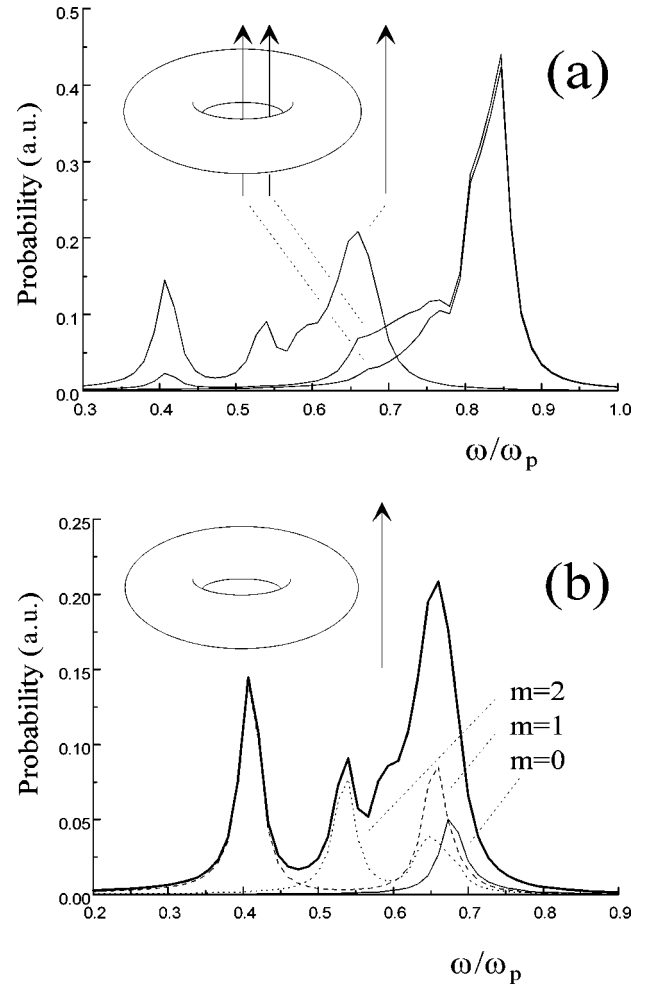


FIG. 9. (a) Loss probability suffered by 100-keV electrons passing near a torus made of Al ($\omega_p = 15.8$ eV and damping $\gamma = 0.5$ eV) following trajectories parallel to the axis of rotational symmetry. The internal and external radii of the toroidal surface are 170 a.u. and 250 a.u., respectively. The impact parameters with respect to the axis of symmetry are 0, 40, and 460 a.u. (see the inset). (b) Contribution of the first m components for the largest impact parameter under consideration.

of the sphere, where for a certain m the allowed modes are those corresponding to $l \geq |m|$, l being the angular momentum number.

V. CONCLUSIONS

The boundary-charge method has been applied to the calculation of low-energy losses of electrons passing near arbitrarily shaped dielectric interfaces. The cases of interfaces characterized by translational invariance along one particular direction and axially symmetric interfaces have been studied in more detail. This increases considerably the number of geometries for which electron-energy-loss calculations are available and at the same time offers the possibility of fitting the shape of objects observed with electron microscopes with respect to the direction of the electron beam. Examples have been offered for wedges, coupled cylinders, coupled spheres, and toroidal surfaces.

Two customary approximations have been adopted. First, the dielectric properties of the different media under consid-

eration have been described in terms of frequency-dependent dielectric functions, appropriate for the large electron velocities of common use in electron microscopy. Furthermore, the dielectrics are assumed to terminate suddenly, defining abrupt interfaces. Concerning this latter point, consecutive layers of increasingly lower electron density are a good candidate to simulate smooth profiles.³⁴ Further research on this point is in progress.

Convergence in the number of points N has been achieved with ≈ 100 points per surface (wedge, cylinder, etc.). Computation times for $N=100$ are in the range of seconds for one value of ω on a Pentium 133 computer. The most time demanding part of the calculation is the inversion of the self-consistent equation (8), which scales as N^3 . The calculation of energy filtered images presents the advantage that it only requires one to solve Eq. (8) once to obtain the boundary

charge, out of which the whole image can be constructed in a time proportional to N^2 times the number of points in the image.

Finally, the loss probability has been expressed in terms of separate contributions, ascribed to the excitation of different oscillation modes. This permits one to obtain a weight function for each of the modes that is independent of the actual choice of dielectric functions.

ACKNOWLEDGMENTS

The authors gratefully acknowledge A. Howie, who inspired the work and provided many helpful suggestions. This work was supported by the Departamento de Educación del Gobierno Vasco, the University of the Basque Country, and Iberdrola SA.

-
- ¹R. H. Ritchie and A. Howie, *Philos. Mag. A* **36**, 463 (1977).
²R. H. Ritchie and A. Howie, *Philos. Mag. A* **58**, 753 (1988).
³E. Fermi, *Phys. Rev.* **57**, 485 (1940).
⁴R. H. Ritchie, *Phys. Rev.* **106**, 874 (1957).
⁵P. M. Echenique and J. B. Pendry, *J. Phys. C* **8**, 2936 (1975).
⁶P. M. Echenique, J. Bausells, and A. Rivacoba, *Phys. Rev. B* **35**, 1521 (1987).
⁷N. Zabala, A. Rivacoba, and P. M. Echenique, *Surf. Sci.* **209**, 465 (1989).
⁸A. Rivacoba, S. P. Apell, and N. Zabala, *Nucl. Instrum. Methods Phys. Res. B* **96**, 465 (1995).
⁹J. M. Pitarke and A. Rivacoba, *Surf. Sci.* **337**, 294 (1997).
¹⁰R. García-Molina, A. Gras-Martí, and R. H. Ritchie, *Phys. Rev. B* **31**, 121 (1985).
¹¹T. L. Ferrell and P. M. Echenique, *Phys. Rev. Lett.* **55**, 1526 (1985).
¹²P. M. Echenique, A. Howie, and D. J. Wheatley, *Philos. Mag. B* **56**, 335 (1987).
¹³J. Aizpurua, A. Rivacoba, and S. P. Apell, *Phys. Rev. B* **54**, 2901 (1996).
¹⁴A. Rivacoba, N. Zabala, and P. M. Echenique, *Phys. Rev. Lett.* **69**, 3362 (1992).
¹⁵N. Zabala and A. Rivacoba, *Phys. Rev. B* **48**, 14534 (1993).
¹⁶M. Schmeits and L. Dambly, *Phys. Rev. B* **44**, 12706 (1991).
¹⁷N. Zabala, A. Rivacoba, and P. M. Echenique, *Phys. Rev. B* **56**, 7623 (1997).
¹⁸M. Schmeits, *Phys. Rev. B* **39**, 7567 (1989).
¹⁹C. A. Brebbia, J. C. Telles, and L. C. Wrobel, *Boundary Element Techniques* (Springer, Berlin, 1984).
²⁰J. C. Maxwell, *Treatise on Electricity and Magnetism* (Dover, New York, 1891).
²¹R. Fuchs, *Phys. Lett.* **48A**, 353 (1974).
²²R. Fuchs, *Phys. Rev. B* **11**, 1732 (1975).
²³F. Ouyang and M. Isaacson, *Philos. Mag. B* **60**, 481 (1989).
²⁴F. Ouyang and M. Isaacson, *Ultramicroscopy* **31**, 345 (1989).
²⁵R. Fuchs (private communication).
²⁶J. Q. Lu and A. A. Maradudin, *Phys. Rev. B* **42**, 11159 (1990).
²⁷R. Goloskie, T. Thio, and L. R. Ram-Mohan, *Comput. Phys.* **10**, 477 (1996).
²⁸S. P. Apell, P. M. Echenique, and R. H. Ritchie, *Ultramicroscopy* **65**, 53 (1996).
²⁹L. C. Davis, *Phys. Rev. B* **14**, 5523 (1976).
³⁰W. H. Press *et al.*, *Numerical Recipes* (Cambridge University Press, New York, 1989).
³¹J. Osma and F. J. García de Abajo, *Phys. Rev. A* **56**, 2032 (1997).
³²L. Dobrzynski and A. A. Maradudin, *Phys. Rev. B* **6**, 3810 (1972).
³³M. Schmeits, *Phys. Rev. B* **39**, 7567 (1989).
³⁴J. E. Inglesfield and E. Wikborg, *J. Phys. F* **5**, 1706 (1975).